Advanced Optical Materials

ADVANCED OPTICAL MATERIALS
www.advopticalmat.de

RESEARCH ARTICLE OPEN ACCESS

Epitaxial $MgSnN_2$ on 4H-SiC (0001): An Earth-Abundant Nitride for Green Optoelectronics and Photovoltaics

D. Gogova[1] | D. Tran[1,2,3] | V. Stanishev[1,4] | D. Shafizadeh[1] | C.-L. Hsiao[1] | M. Kim[1,2,5] | B. Pécz[6] | A. Kovács[6,7] | K. Frey[8] | A. Sulyok[6] | N. K. Singh[1,9] | A. Le Febvrier[1,9] | P. Eklund[1,9] | V. Darakchieva[1,2,4,5]

[1]Department of Physics, Chemistry and Biology, Linköping University, Linköping, Sweden | [2]Center for III-Nitride Technology – C3NiT-Janzèn, Linköping University, Linköping, Sweden | [3]Department of Electrical Engineering, Stanford University, Stanford, California, USA | [4]NanoLund, Center for III-Nitride Technology – C3NiT-Janzèn, Terahertz Materials Analysis Center, THeMAC and Division of Solid State Physics, Lund University, Lund, Sweden | [5]Wallenberg Initiative Materials Science for Sustainability (WISE), Department of Physics, Chemistry and Biology (IFM), Linköping University, Linköping, Sweden | [6]HUN-REN Centre for Energy Research, Institute of Technical Physics and Materials Science, Budapest, Hungary | [7]Ernst Ruska-Centre for Microscopy and Spectroscopy with Electrons, Forschungszentrum Jülich, Jülich, Germany | [8]HUN-REN Centre for Energy Research, Institute of Energy Security and Environmental Safety, Budapest, Hungary | [9]Department of Chemistry – Angström, Uppsala University, Uppsala, Sweden

Correspondence: D. Gogova (daniela.gogova@liu.se)

Received: 19 March 2026 | **Revised:** 16 August 2026 | **Accepted:** 21 August 2026

Keywords: epitaxy | materials science | nitride | optoelectronics | photoluminescence | photovoltaics | semiconductor | sputter deposition | thin film | wurtzite crystal structure

ABSTRACT

Group II–IV-Nitrides has emerged as a novel class of Earth-abundant semiconductors. Owing to their tunable bandgaps these materials are attractive candidates for replacing expensive Ga-based alloys in photovoltaics and green-gap optoelectronics. In this work, epitaxial growth of $MgSnN_2$ thin films on 4H-SiC (0001) substrates by direct current magnetron sputtering is demonstrated. Mg and Sn metal targets were co-sputtered in a nitrogen-containing atmosphere at growth temperatures up to 500 °C. The film composition is varied from Sn-rich to stoichiometric and Mg-rich regimes. X-ray diffraction and cross-sectional transmission electron microscopy confirm the $MgSnN_2$ layers grow epitaxially in a wurtzite crystal structure, exhibiting the epitaxial relationships with the substrate: $MgSnN_2$ [0001]//4H-SiC [0001] and $MgSnN_2$ [10$\bar{1}$0]//4H-SiC[10$\bar{1}$0]. Improved crystalline quality is observed for higher deposition temperatures and stoichiometric composition, as evidenced by the narrowing of rocking curve's linewidths. Optical characterization reveals a high absorption coefficient (~10^5 cm^{-1}) in the visible spectrum. Photoluminescence measurements show emission peaked at ~2.4 eV, highly desirable for optoelectronic devices in the challenging green spectral region. These results establish $MgSnN_2$ as an earth-abundant, environmentally-friendly material, structurally compatible with III-nitrides, with potential for cost-efficient components in sustainable optoelectronics and photovoltaics.

1 | Introduction

The importance of photovoltaics and optoelectronics based on new earth-abundant materials should be seen in the perspective of the ever-growing energy demand of mankind and the need to address it with sustainable material technology. During the last decades, III-nitrides revolutionized solid-state lighting and power electronics [1–6]. Expanding the nitride semiconductor family by including the II–IV ternary nitrides [7–16] offers an exciting opportunity for materials and device design that may help to overcome some of the limitations of the III-Ns, to replace the rare and very expensive gallium and indium

in novel light-emitting diodes (LEDs) for the visible spectral range.

$Mg(Zn)SnN_2$ was first theoretically predicted in 2016 [17] and reported to be experimentally obtained in 2019, without any details for the method and technological parameters employed [18], demonstrating their tunability in the range of 1.45–3.5 eV. Ternary heterovalent II–IV-N_2, especially $MgSnN_2$, semiconductors have some advantages over group-III nitride alloys such as InGaN, which are the primary materials employed today in optoelectronics and photonics [1–6]: (i) composed of earth-abundant elements, i.e., $MgSnN_2$ is an inexpensive material, because Mg and Sn are significantly less expensive than In and Ga and they benefit from a mature recycling infrastructure; (ii) $MgSnN_2$ has the potential to avoid phase separation in the whole alloy composition range [15], unlike InGaN [19], and (iii) $MgSnN_2$ and related II–IV-N_2 can be synthesized at significantly lower deposition temperatures [7–16], i.e., their fabrication is more cost-effective and energy efficient than that of III-Ns. The ternary $MgSnN_2$ is also a nontoxic and stable compound at ambient conditions and hence offers additional advantages with respect to other emerging promising materials for optoelectronics and photovoltaics such as perovskites, which are either unstable or contain Pb.

Furthermore, the variety of wurtzite-type semiconductors with band gaps of 1.8–2.5 eV is limited, which hinders bridging the so-called "green gap" [20] associated with the low efficiency of InGaN-based light-emitting diodes in the green spectral range. The disordered wurtzite-type $MgSnN_2$ has been shown to have a direct band gap of ~2.3 eV and it is a potential candidate for green emitters in LEDs [15].

Hypothetically, the ideal $MgSnN_2$ structure (similar to ZnSn(Si, Ge)N_2) can be derived from a GaN crystal by replacing every two Ga atoms with one Mg atom and one Sn atom. Thus, $MgSnN_2$ and related II–IV–N_2 compounds have an additional degree of freedom in comparison to III-Nitrides accessible through the symmetry of the cation sublattice. The state of existing of two different valence cations (Mg^{2+} and Sn^{4+}) offers a unique possibility to tune the material electronic, electrical, and optical properties by means of controlling the degree of cation site ordering for a fixed stoichiometric formula [21].

Since $MgSnN_2$ is a new material, there are only a few experimental publications in the literature. Pseudo-bulk $MgSnN_2$ in a powder form, has been synthesized by using a high-pressure metathesis reaction [22]. $MgSnN_2$ thin films with different degrees of crystallinity and crystallographic structures (wurtzite-type and metastable rocksalt-like) have been demonstrated by PE-MBE on yttria-stabilized zirconia (111) substrates [23] (epitaxy proved only by in situ RHEED study) and RF-sputtering of metal or composite targets on fused silica, Si, sapphire (0002), MgO (111), and sapphire with a GaN buffer layer (0002) substrates [14–16, 24]. Epitaxial rocksalt (rs) $MgSnN_2$ thin films were grown on cubic MgO (111) substrates at lower temperatures (about 100°C) and their structure comprised small crystalline grains [25]. This rock salt phase is metastable since it turns into wurtzite-phase when annealed at 400°C for 5 h in N_2 at ambient pressure [25]. Despite the growing interest in $MgSnN_2$, epitaxial growth has so far been demonstrated on only a limited number of substrates with the best crystalline quality achieved on GaN-buffered sapphire via RF-sputtering of Mg—Sn composite target in a nitrogen atmosphere [14, 15]. However, the technology development in general is still in its infancy due to the relatively low crystalline quality of the $MgSnN_2$ thin films (a result of predominant employment of the non-equilibrium sputtering method on substrates with large lattice parameters mismatchs at low synthesis temperatures), motivating the need for considerable material improvement by epitaxial growth on lattice- and thermally matched substrates.

The development of $MgSnN_2$ for practical optoelectronic and photovoltaic applications requires not only improvements in crystalline quality but also the establishment of technologically relevant epitaxial platforms compatible with existing semiconductor technologies. High-quality epitaxial layers are essential because they enable reliable determination of the intrinsic structural, optical, and electrical properties of the material while providing the foundation for future device fabrication.

In this work, we demonstrate direct-current magnetron sputter epitaxy of high-quality wurtzite $MgSnN_2$ on 4H-SiC(0001), a substrate widely used for III-nitride electronics and optoelectronics [26–28]. We establish the epitaxial relationship between $MgSnN_2$ and the 4H-SiC substrate, demonstrating its structural compatibility with the III-nitride materials platform, and correlate the growth conditions with the structural, optical, and electrical properties of the films. By demonstrating strong visible-light absorption together with green photoluminescence, this work identifies $MgSnN_2$ as a promising earth-abundant semiconductor for sustainable optoelectronic and photovoltaic technologies while providing a pathway toward its future integration with mature III-nitride platforms.

2 | Results and Discussion

The growth window for $MgSnN_2$ thin films with different structures (polycrystalline, textured, and epitaxial) is relatively wide, i.e., the deposition temperature can be varied from room temperature to 500°C [24]. To get highly oriented material on 4H-SiC (0001) we have focused on the temperature range 350°C–500°C. The deposition rate was determined to be 5.9–5.7 nm/min at 350°C, 5.4 nm/min at 400°C, 5.5–5.8 nm/min at 450°C, and 5.3–5.6 nm/min at 500°C. The variations in the DC power ratio on the metal electrodes were used to fine tune the cation ratio (semiconductor compound composition).

2.1 | Cation Ratio

EDS measurements performed in the SEM microscope identify the cation ratio (layer composition), which varied from Sn-rich ($0.6 \leq x < 1$) to stoichiometric ($x = 1$) and slightly Mg-rich ($1 < x \leq 1.2$). Following growth optimization, stoichiometric $MgSnN_2$ composition corresponding to 25 at.% Mg, 25 at.% Sn, and 50 at.% N was confirmed for films grown at 400°C and 450°C using an applied Mg-to-Sn target power ratio of 49:11 W. No other impurities were detected in the as-grown layers with the sensitivity of the EDS. However, we cannot rule out eventual

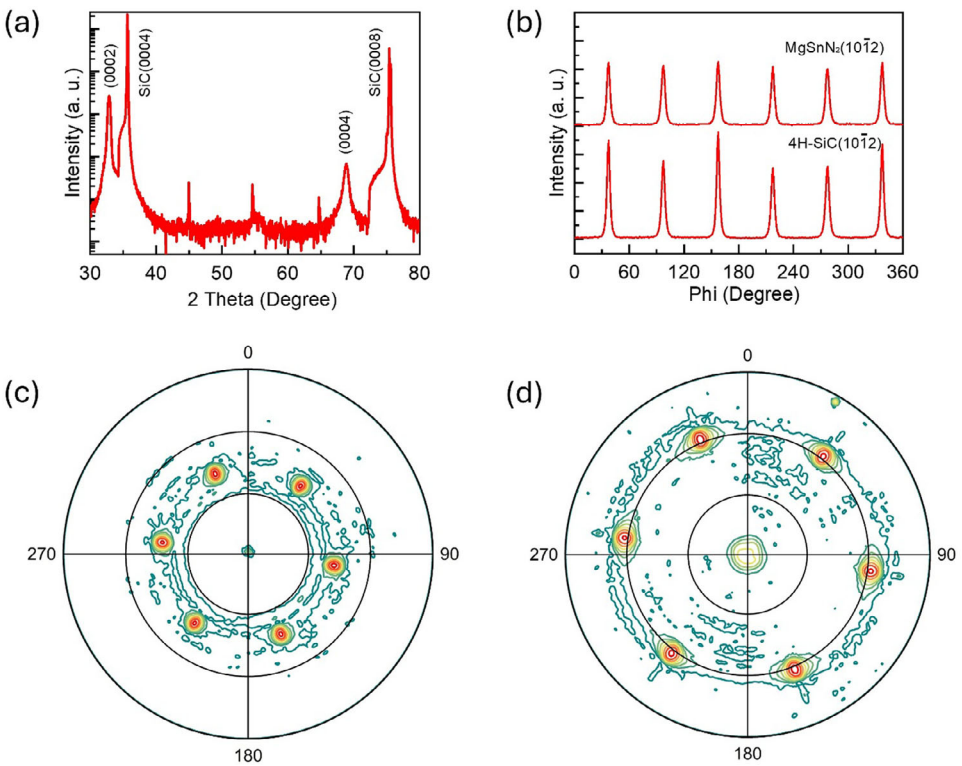

FIGURE 1 | XRD measurements of stoichiometric $MgSnN_2$ grown on 4H-SiC (0001) substrate in the temperature range 350°C–450°C. (a) $\theta/2\theta$-scan, (b) φ-scan, and pole figures of (c) 10$\bar{1}$2 $MgSnN_2$ and (d) 10$\bar{1}$2 4H-SiC reflections.

oxygen contamination typical for III-nitrides grown by sputtering as well as for other II–IV-Nitride such as $ZnSnN_2$ [11].

2.2 | Structural Properties

The films' structural properties were studied by XRD $\theta/2\theta$-scans, φ-scans, and pole-figures. A $\theta/2\theta$-scan, typical of stoichiometric $MgSnN_2$ grown at temperatures 350°C–450°C on 4H-SiC (0001), is illustrated in Figure 1. The intense and narrow peak at 2θ = 32.85°, can be assigned to the (0002) Bragg reflection while that at 2θ = 68.86° to the (0004) reflection of the wurtzite $MgSnN_2$ [29]. The $\theta/2\theta$ scan also reveals two intense substrate peaks – the (0004) reflection of 4H-SiC is situated at 35.60°, and the (0008) one at 75.41°. In addition, three small peaks become visible between the main peaks and are attributed to SiC {000l}, which are forbidden reflections, owing to multiple scattering in the substrate. To further study the epitaxial relationship between the $MgSnN_2$ film and SiC substrate, φ-scan XRD and pole figure measurement were employed. Figure 1b shows azimuthal φ-scans acquired at 2θ = 44.93° and 34.07°, corresponding to the $MgSnN_2$ (1012) and 4H-SiC (1012) reflections, respectively, displayed in the upper and lower panels. During the measurements, the sample was tilted by a fixed ψ angle of approximately 44° for the film and 61° for the substrate, while the azimuthal angle φ was rotated at the selected 2θ position. Six peaks were obtained at the respective Ψ -angles with an azimuth separation of 60° in both measurements for the layer and the substrate. The φ-scans reveal excellent alignment between the $MgSnN_2$(10$\bar{1}$2) and 4H-SiC (10$\bar{1}$2). To verify if there are any other misoriented grains embedded in the film, XRD pole figures were measured at (a) 10$\bar{1}$2 $MgSnN_2$ and (b) 10$\bar{1}$2 4H-SiC reflections, displayed in Figure 1c,d, respectively. Six distinct reflections located at Ψ angle ~44° and 61° can be seen in Figure 1c,d, respectively, which are attributed to the six-fold symmetry of the hexagonal structure. No other distinct peaks were observed in both pole figures, indicating that the $MgSnN_2$ layer grew epitaxially on the 4H-SiC substrate. Thus, a well-defined epitaxial relationship of $MgSnN_2$ [0001]//4H-SiC [0001] and $MgSnN_2$ [10$\bar{1}$0]//4H-SiC [10$\bar{1}$0] can be obtained. These results confirm the epitaxial growth of c-plane–oriented $MgSnN_2$ layers with a hexagonal wurtzite structure, demonstrating structural compatibility with group-III nitrides, which is important for applications in optoelectronics. Although wurtzite $MgSnN_2$ is commonly associated with Mg-rich growth conditions due to the higher ionicity of Mg—N bonds compared to Sn—N and Zn—N bonds, we observed the wurtzite crystallographic structure even for stoichiometric and Sn-rich epitaxial layers.

The effect of the growth temperature and composition on the structural quality of the $Mg_xSn_{2-x}N_2$ epitaxial layers is illustrated in Figure 2. As shown in Figure 2a, the layers grown in the temperature range of 350°C–450°C with stoichiometric, close to stoichiometric and slightly Mg-rich composition exhibit a wurtzite (wz) phase with (0002) orientation. No other (e.g., metal, Mg—N, and Sn—N) phase or additional grain orientation was observed. At a growth temperature of 500°C and Sn-rich layer composition, the main growth direction remains unchanged; however, the layer incorporates additional m-plane oriented crystal domains, indicated by the presence of (10$\bar{1}$0) and (20$\bar{2}$0) diffraction peaks at 2θ of 30.6° and 63.7°, respectively. The lattice constants of the c-plane crystals, measured using the (0002) and

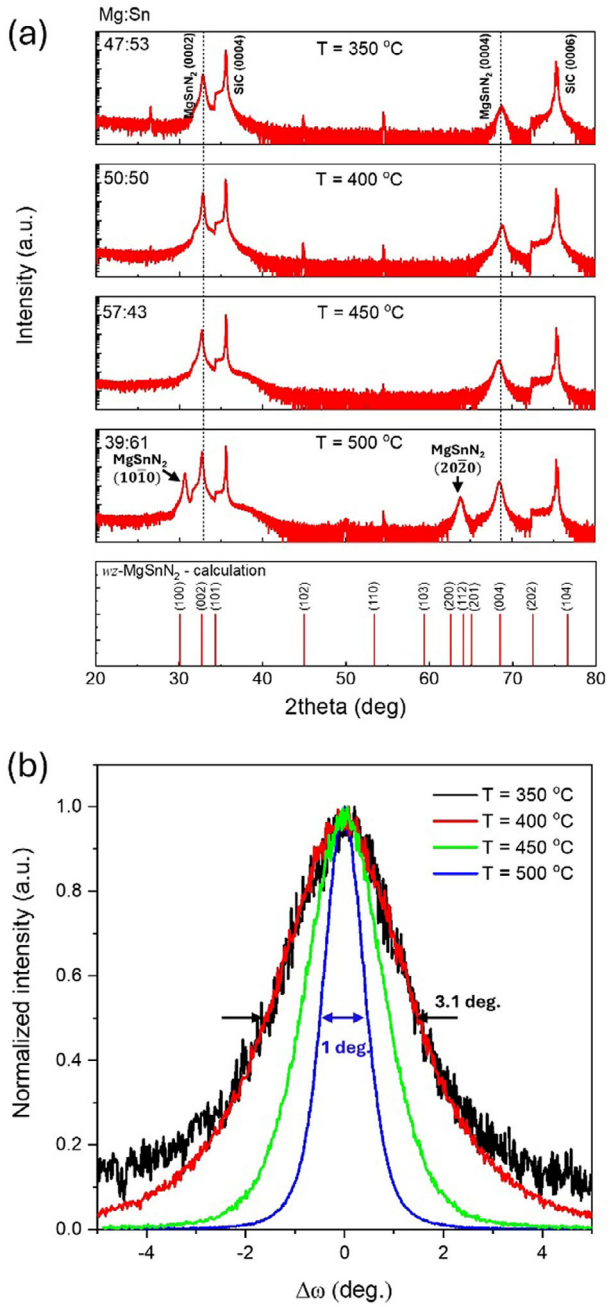

FIGURE 2 | (a) $2\theta/\theta$ scans of the *wz*-$Mg_xSn_{2-x}N_2$ layers grown at temperatures in the range of 350°C–500°C, the XRD spectrum theoretically calculated for stoichiometric $MgSnN_2$ is also shown, (b) (10$\bar{1}$2) RCs of the corresponding layers reported in (a).

(10$\bar{1}$2) diffractions, are found to be $a = 0.349$ and $c = 0.547$ nm. Calculations using both (10$\bar{1}$0) and (20$\bar{2}$0) diffractions yield the same value of $a = 0.337$ nm for the m-plane crystals. At this high temperature, the layer becomes more Sn-rich with Mg:Sn cation ratio of 39:61. This behavior is attributed to the increased volatility of Mg at higher growth temperatures.

Despite the large variation in the layers' cation ratio with growth temperature, the XRD peaks of (0002) and (0004) diffractions remain almost unchanged and aligned well with the corresponding peak positions of the powder diffraction pattern for stoichiometric $MgSnN_2$. Despite the variation in the Mg-to-Sn ratio from 47:53 to 57:43 with increasing growth temperature, the XRD peak position remains nearly unchanged. This behavior can be attributed to the similar ionic radii of tetrahedrally coordinated Mg^{2+} (57 pm) and Sn^{2+} (55 pm), which lead to only minor changes in the lattice parameters with composition [14]. Furthermore, the observed variation in composition is relatively modest resulting in lattice parameter changes below the detection limit of the XRD measurements.

The XRD powder diffraction pattern was generated by us employing Vesta (3D visualization program designed for crystallography, materials science, and chemistry), with cell parameters of the disordered wz-$MgSnN_2$ obtained from electronic calculation and structural optimization using density functional theory, yielding $a = 0.3426$ and $c = 0.5474$ nm [29]. Notably, the (10$\bar{1}$0) and (20$\bar{2}$0) peak positions significantly differ from those of the reference pattern by +0.52° and +1.3°, due to the differences in the lattice constant *a*. Interestingly, the lattice constant *a* of the c-plane and m-plane domains in the layer are significantly different, which could be associated with differences in (i) the strain states and/or (ii) the cation ratio of these two different types of crystal domains. Figure 2b presents the (10$\bar{1}$2) rocking curves (RCs) of the $Mg_xSn_{2-x}N_2$ layers. The RC full width at half maximum (FWHM) is as large as 3.1° for the layer grown at T = 350°C, while higher growth temperatures result in progressively narrower linewidths. In particular, the minimum FWHM of 1° is obtained for the layer grown at T = 500°C. The result indicates better crystalline quality of the individual domains at higher growth temperatures up to 500°C.

Interestingly, the secondary m-plane orientation is observed only for the highest growth temperature and the largest deviation from stoichiometry, suggesting that its formation is governed by the combined effects of growth temperature and surface composition. A possible explanation is that the higher temperature increases adatom mobility while the increased Mg loss under Sn-rich conditions alters the surface stoichiometry, consequently, and the relative stability of competing nuclei. This may reduce the energetic preference for *c*-plane nucleation during the initial stages of growth, allowing *m*-plane-oriented domains to form. Once nucleated, these domains continue to grow, resulting in the observed textured film. However, this interpretation remains speculative and dedicated experimental and theoretical studies are required to elucidate the underlying growth mechanism. In addition, to further suppress the secondary-oriented grains while preserving good crystalline quality, further optimization of the initial nucleation stage is required. Possible strategies include using a growth temperature below the onset of secondary-orientation formation, introducing a thin low-temperature nucleation layer followed by moderate-temperature growth, reducing the deposition rate, and improving the substrate surface preparation prior to deposition as accomplished for III-nitrides or some technology-relevant oxides [31–36].

Due to the appearance of m-plane crystal phase orientation for the Sn-rich sample and the enhanced Mg volatility at higher temperatures the deposition temperature was not further increased in our series of experiments. RCs for $Mg_xSn_{2-x}N_2$ epitaxial layers have not yet been reported in the literature, preventing a direct comparison. Although the RC's are broader than those typically

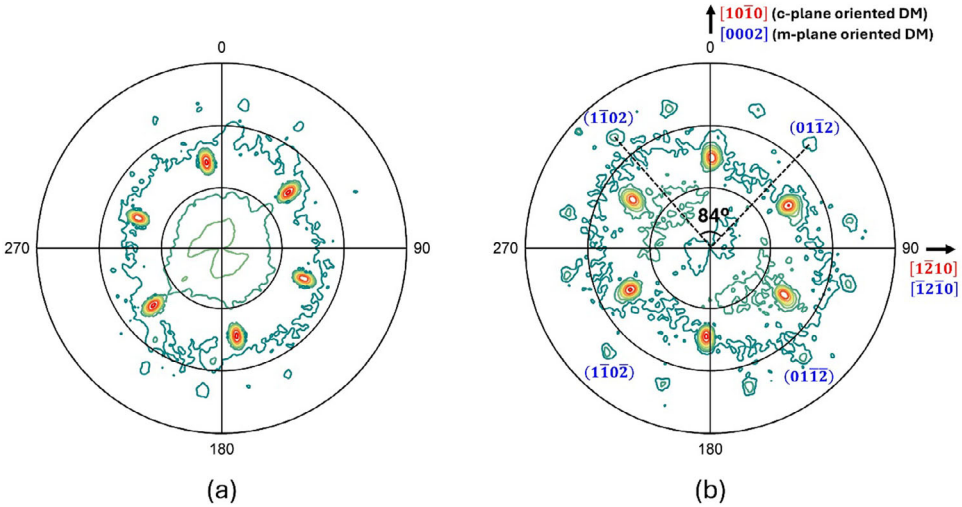

FIGURE 3 | Pole figures of {10$\bar{1}$2} diffractions measured for the $MgSnN_2$ layers grown at two different temperatures of T = 450°C and cation ratio 57:43 – (a) and T = 500°C, cation ratio of 39:61 – (b). The mutual orientations marked for the *c*-plane and *m*-plane oriented domains are in red and blue, respectively.

reported for mature III-nitride epitaxy [28, 30, 31], which has benefited from approximately six decades of optimization, they are consistent with the observed single-phase epitaxial growth and indicate very good crystalline quality within the current state of the emerging $Mg_xSn_{2-x}N_2$ epitaxy.

The pole figure of the layer grown at T = 450°C and cation ratio of 57:43 contains six peaks at an inclination angle of 44°, corresponding to {10$\bar{1}$2} reflections of *c*-plane-oriented wurtzite crystal, revealing the expected six-fold symmetry of the lattice (see Figure 3a). The layer grown at T = 500°C and a cation ratio of 39:61 additionally shows 12 peaks at an inclination angle of Ψ = 71.5°, which have significantly lower intensity compared to the main peaks. The extra peaks match the {10$\bar{1}$2} reflections characteristic of *m*-plane (1-100) oriented crystals, indicating the coexistence of both *c*-plane and *m*-plane domains in the layer grown at 500°C, with the *m*-plane component being minor (Figure 3b). For the m-plane domains, the measured reflections particularly correspond to (01$\bar{1}$2), (1$\bar{1}$02), (01$\bar{1}\bar{2}$), and (1$\bar{1}$0$\bar{2}$) planes. The first and second reflections form an azimuth angle of 84°, while it is 96° for the first and third ones. The full set of 12 peaks arises from a 60° rotation repetition of the *m*-plane oriented domain. Notably, the results indicate that the c-axis of the *m*-plane domains aligns along the ⟨10$\bar{1}$0⟩ direction of the *c*-plane host domains.

The structure of the stoichiometric $MgSnN_2$ layer grown at a temperature of 400°C was further studied in cross-sectional geometry as illustrated in Figure 4, by preparing a thin specimen using FIB. The BF STEM image in Figure 4a shows the columnar structure of the $MgSnN_2$ layer, which nucleates at the 4H-SiC (0001) surface. The layer thickness is approximately 600 nm and the lateral dimension of the columns is in the range of 60–80 nm. The epitaxial relationship between $MgSnN_2$ and 4H-SiC is confirmed as $MgSnN_2$[0001]//4H-SiC [0001] and $MgSnN_2$ [10$\bar{1}$0]//4H-SiC [10$\bar{1}$0] using a selected area electron diffraction (SAED) pattern recorded from the interface region. Chemical composition measurement using EDS (Figure 4c) reveals a composition of Mg – 28 at.%, Sn – 25 at.%, and N – 47 at.%. These values are in good agreement with the EDS measurement obtained from the bulk sample using SEM. Figure 4d shows a high-resolution BF STEM image of the $MgSnN_2$ layer acquired from the mid-section confirming the single-crystalline nature of the column. The interface structure is presented in Figure 4e, where $MgSnN_2$ grains are observed to nucleate and grow epitaxially on the 4H-SiC substrate. The interface between the substrate and the layer was further investigated with element-sensitive high-angle annular dark-field (HAADF) STEM imaging, as shown in Figure 4f, where the intensity scales approximately as $I \sim Z^2$. A 1–2 ML thick region of dark contrast at the interface indicates a high concentration of light elements such as C, O, or N. Next to the HAADF STEM image, the unit cells of the wz-$MgSnN_2$ and 4H-SiC (0001) are shown to illustrate the epitaxial relationship.

2.3 | Optical Properties

Figure 5 shows the absorption coefficient spectra, extracted from spectroscopic ellipsometry measurements, for a set of wurtzite highly oriented $MgSnN_2$ layers with different stoichiometry/cation ratios. The absorption coefficients for all layers are in the high 10^4 range up to $\sim 10^5$ cm^{-1} in the visible spectrum, i.e., values approaching those of the solar-energy-relevant GaAs [9]. Such experimentally derived values are not reported so far in the literature. Recent theoretically calculated absorption coefficient and reflectivity curves of $MgSnN_2$ validate that the disordered rock-salt structure might be used as an absorber layer in the higher energy region of the visible spectrum in tandem solar devices [9], whereas the disordered wurtzite and orthorhombic crystal structures could serve as window layers of solar cells. However, our results demonstrate that highly ordered epitaxial $MgSnN_2$ layers with a wurtzite structure have large absorption coefficients too.

The optical band gap can also be extracted from ellipsometry or transmission-reflection measurements. However, in heavily doped semiconductors, it may appear larger than the electronic band gap because the lowest conduction-band states are already occupied, forcing optical transitions to higher-energy states. This

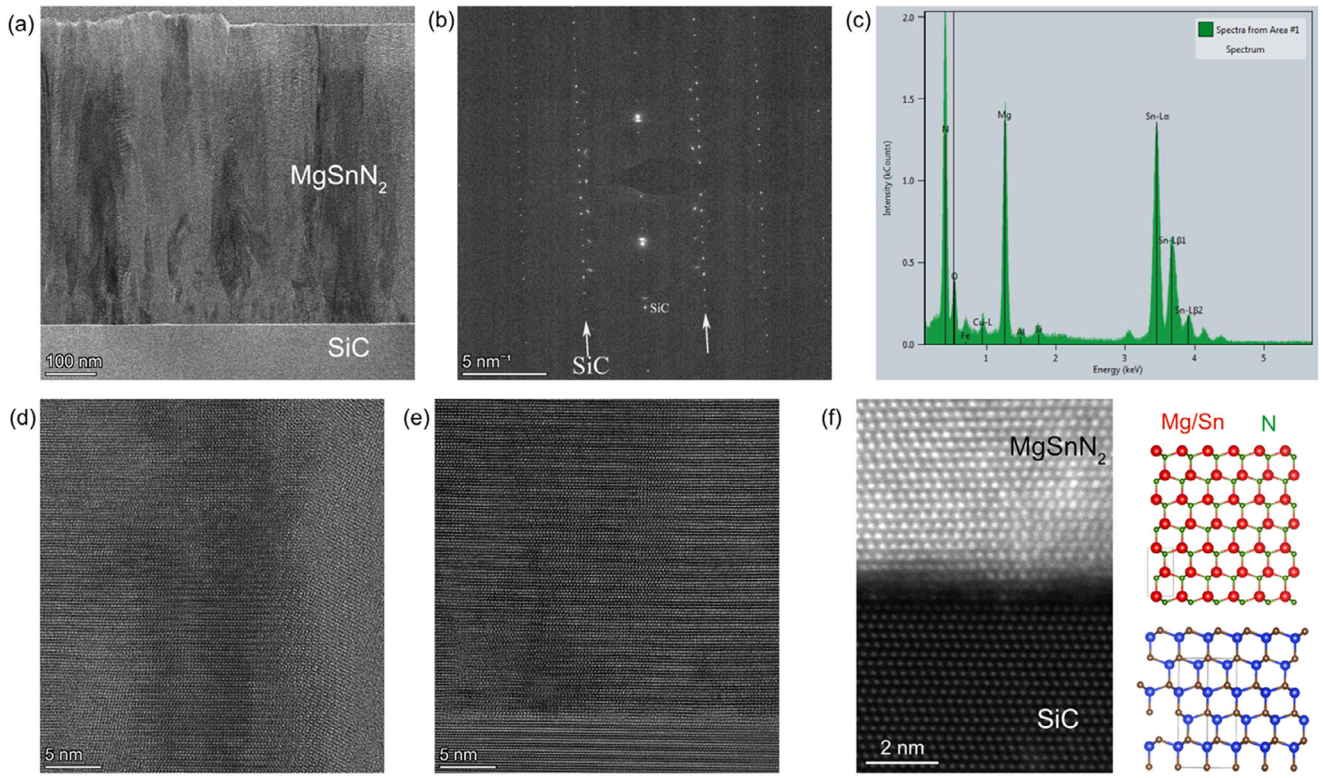

FIGURE 4 | (a) BF STEM image showing the columnar structure of the $MgSnN_2$ layer on 4H-SiC substrate. The Pt/C protective layer deposited during the FIB preparation is visible on the top. (b) SAED pattern recorded from the interface region showing the epitaxial relationship of wz-$MgSnN_2$ and 4H-SiC (0001). (c) EDS spectrum recorded from the $MgSnN_2$ layer. (d, e) BF STEM images of the $MgSnN_2$ layer and interface regions, respectively. (f) HAADF STEM image of the interface and the atomic arrangements of wz-$MgSnN_2$ and 4H-SiC.

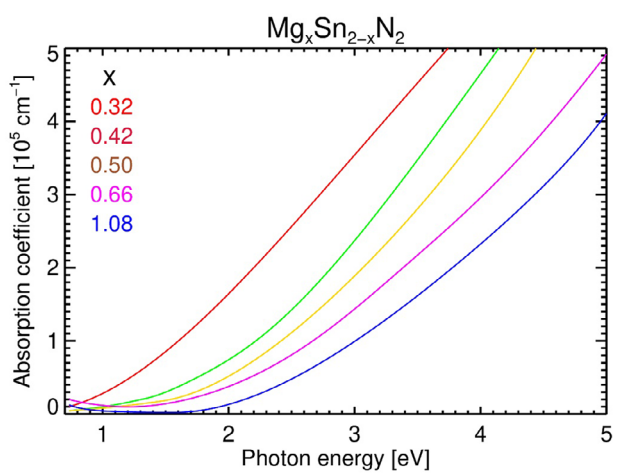

FIGURE 5 | Absorption coefficient spectra vs photon energy of a set of wurtzite highly oriented $Mg_xSn_{2-x}N_2$ layers with different stoichiometry (x = 0.32; 0.42; 0,50; 0.66; 1.08).

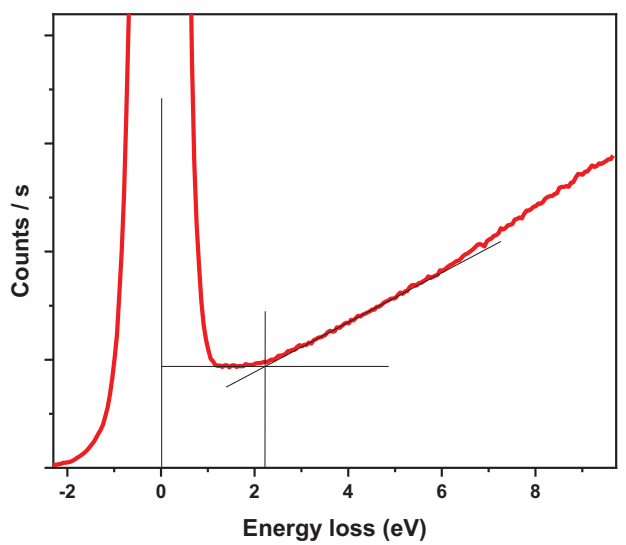

FIGURE 6 | A typical REELS spectrum of a stoichiometric $MgSnN_2$ layer deposited on 4H-SiC (0001) substrate.

Burstein-Moss effect. We previously reported such overestimated optical band-gap values for $ZnSnN_2$ [12]. Therefore, in the present study, reflection electron energy loss spectroscopy (REELS) was employed to determine the fundamental band gap, as it is less affected by band filling than optical methods.

Prior to the measurements, the oxygen adsorbed on the surface of the as-grown samples, kept at ambient conditions, was removed in several steps via Ar ion sputtering controlled by Auger electron spectroscopy. A typical REELS spectrum of a stoichiometric wz-$MgSnN_2$ layer deposited onto 4H-SiC (0001) substrate is depicted in Figure 6. Since the elastic peak is three orders of magnitude more intense, accurately measuring the low-intensity loss region of the spectrum required extended averaging. The average of 10 spectra was used for the $MgSnN_2$ band gap estimation. The

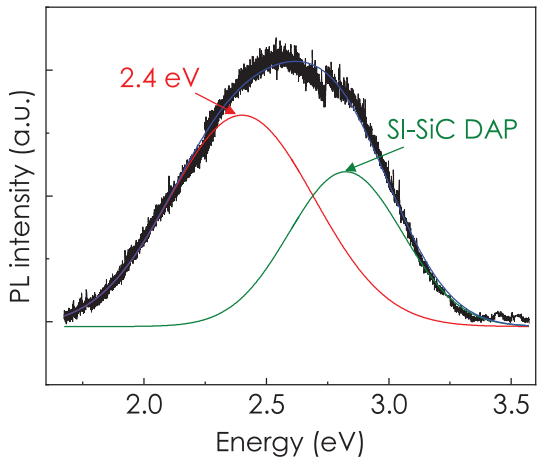

FIGURE 7 | A low-temperature photoluminescence spectrum typical of an epitaxial $MgSnN_2$ sample.

band gap value of epitaxial material was determined to be 2.24 ± 0.1 eV. Optical band gap values ranging from 2.27 to 2.43 eV have been reported in the literature for the direct bandgap stoichiometric $MgSnN_2$ thin films with a different degree of crystallinity [13–15, 24].

A low-temperature photoluminescence spectrum, measured at 80 K with a UV laser excitation of 351 nm, typical of a $MgSnN_2$ sample is illustrated in Figure 7. The PL peak at 2.85 eV is identified as the N-Al donor–acceptor pair (DAP) emission of SI-SiC [40] appearing at low-temperatures, while the peak at 2.4 eV is due to the $MgSnN_2$. Obviously, the material grown has a green-light photoluminescence with a peak maximum at 2.4 eV and therefore is promising for a source in optically active devices for the critical up-to-date green gap [20]. Direct bandgap semiconductors with bandgaps in this range are strongly needed for the development of green LEDs since the large Indium (In) content in the present green light InGaN-based LEDs leads to decreased efficiency due to the In-phase segregation appearing at large In contents in the InGaN alloy [19]. The indium segregation principally originates from the large lattice mismatch between InN and GaN.

Additionally, the wurtzite $MgSnN_2$ (0001) could be integrated with the well-developed III-nitride semiconductors because of their structural compatibility. Moreover, such direct bandgaps [15, 29] are required for top cells in high-efficiency tandem solar cells.

Electrical Hall effect measurements performed on a series of $MgSnN_2$ samples showed high electron concentration reaching 4.7×10^{19} cm^{-3} for stoichiometric films and 4.3×10^{20} cm^{-3} for Sn-rich layers. The corresponding electron mobilities range from 3.3 to 5.9 $cm^2/V{\cdot}s$. These values are consistent with earlier reports in the literature [22, 29, 37]. Such high electron concentrations lead to a Burstein-Moss shift of the optical transition energy, accounting for the difference between the REELS-derived band gap of 2.24 eV and the PL peak maximum at ≈2.4 eV.

First principle calculations have shown that wurtzite $MgSnN_2$ exhibits self-doped *n*-type conductivity, and the antisite defect Sn_{Mg} was suggested to be the primary source of free electrons [38].

The propensity for forming the stoichiometry preserving $Mg_{Sn}+Sn_{Mg}$ defect complex leads to cation disorder in $MgSnN_2$, which induces a bandgap reduction because of a violation of the octet rule [39]. The cation-size mismatch has been suggested to be the reason for structural distortion, configurational disorder, and valence-band splitting in II–IV-N_2 semiconductors [39]. However, the unintentional high free electron concentration could be also due to oxygen contamination, which is inevitably present in nitride semiconductors and has been detected in sputtered $ZnSnN_2$ by SIMS [11].

The unintentionally high electron concentration in as-grown $MgSnN_2$ still remains a scientific and technological challenge and additional study is needed to clarify its nature. Nevertheless, n-type $MgSnN_2$ could be integrated with established p-type semiconductors, such as p-GaN or p—Si, depending on the targeted device application.

3 | Conclusions

We have demonstrated direct-current magnetron sputter epitaxy of wurtzite $MgSnN_2$ on 4H-SiC(0001) substrates, establishing its structural compatibility with the group-III nitride materials platform. X-ray diffraction and cross-sectional TEM measurements confirm the epitaxial growth of the hexagonal phase, exhibiting an epitaxial relationship with the substrate described by: $MgSnN_2[0001]//4H\text{-}SiC\ [0001]$ and $MgSnN_2\ [10\bar{1}0]//4H\text{-}SiC[10\bar{1}0]$. The crystalline quality improves by increasing the deposition temperature up to ≈ 500°C and for stoichiometric composition. The experimentally determined absorption coefficient reaches $\approx 10^5$ cm^{-1} in the visible range of the spectrum, i.e., demonstrating the potential of $MgSnN_2$ as an absorber in tandem solar cells. Furthermore, the observation of green-light photoluminescence with a peak maximum at ≈2.4 eV highlights the potential of $MgSnN_2$ for optically active devices addressing the challenging green spectral region. These results establish $MgSnN_2$ as an earth-abundant semiconductor compatible with III-Nitride technologies and provide an important foundation for future optoelectronic and photovoltaic applications.

4 | Experimental Section

$Mg_xSn_{2-x}N_2$ thin films with a wide compositional x-range ($0.6 \leq x \leq 1.2$) were deposited by a DC reactive magnetron co-sputtering of metal Mg (99.995 vol.%) and Sn (99.995 vol.%) targets in an N_2-containing atmosphere employing an ultra-high vacuum Magnetron Sputter deposition chamber with a base pressure of $\sim 5.33 \times 10^{-7}$ Pa. (see for details). The magnetron assemblies were situated on the bottom lid of the chamber each 90° degrees in a co-focal position with an off-axis position of 30°. The target diameter was 50 mm and the distance between the targets and the substrate holder was approximately 135 mm [41]. For all deposition experiments a mixture of N_2 (99.999%) and Ar (99.999%) was used as a sputter gas in the thin film synthesis. The substrates with lateral sizes 10 × 10 mm or 10 × 5 mm were cleaned in an ultrasonic bath as follows: 5 min in acetone, 5 min in propanol, 5 min in deionized water and finally dried in a N_2-flow of high purity. $MgSnN_2$ films were co-sputtered on 4H-SiC (0001). The deposition temperature in a series of experiments varied from

200°C to 500°C with a step of 50°C, in a nitrogen-containing atmosphere with Ar addition. The N_2 flow was 72 sccm, the Ar flow 18 sccm, and the sputtering pressure was fixed at 0.48 Pa. The $MgSnN_2$ films prepared were nominally undoped. The crystalline structures and epitaxial relationship were analyzed by $\theta/2\theta$-scan, φ-scan, and pole-figure x-ray diffraction (XRD) employing a PANalytical Empyrean X-ray diffractometer with a Cu-Kα source and a parabolic mirror as the primary optics and a 0.27° parallel plate collimator as the secondary optics. The thin film thickness was determined by means of a Scanning electron Microscope (SEM) Zeiss, Sigma 300, while the films composition – by Energy dispersive X-ray spectroscopy (EDS) in the SEM.

The cross-sectional specimens for transmission electron microscopy (TEM) studies were prepared using focused Ga ion beam (FIB) sputtering in a dual beam scanning electron microscope (ThermoFisher Scios 2) following a conventional lift-out method. To study the structure and epitaxy of $MgSnN_2$ films, electron diffraction patterns and bright field images were recorded using an aberration-corrected electron microscope (ThermoFisher Themis 200) operated at 200 kV acceleration voltage. The chemical element distribution was measured by EDS and scanning TEM (STEM). The TEM data was processed using Velox software (ThermoFisher).

Reflection electron energy loss spectroscopy (REELS) for band gap measurement was carried on layers grown on 4H-SiC. Since the REELS measurement is a surface-sensitive technique an oxidized region at the sample surface was removed by ion sputtering before the REELS spectra were recorded. For this purpose, low-energy ions sputtering was carried out with 1 keV Ar ion beam scanned over a 2 mm spot at the surface. The REELS spectra were detected using an Escalab Xi+ (Thermo Fisher) equipment and its low-temperature electron source with a low-energy width of the exciting beam was used. Measurements took place at 1 keV primary energy detecting 300 μm spots of the surface observing. Both primary electrons and escaping electrons are related to the surface plane at normal-angle conditions. The spectra were detected at 0.05 eV steps with 0.5 eV energy resolution of the analyzer.

Spectroscopic ellipsometry (SE) using a dual-rotating compensator ellipsometer (RC2, J.A. Woollam Co., Inc.) was performed in the range from 0.75 to 5.9 eV for the characterization of sample optical properties. Psi and Delta spectra were measured at angles of incidence from 45° to 75° with a step of 5°. The experimental data are analyzed using the WVase32 software (J.A. Woollam Co. Inc.) employing a stratified optical model with parametrized model dielectric functions (MDFs) assigned to each layer. The MDF of 4H-SiC was determined from measurements of a bare substrate and was kept fixed during the analysis. The MDF of the $MgSnN_2$ film was modeled as a sum of one Tauc-Lorentz and two Lorentz oscillators. The film thickness and the parameters of the oscillators were determined by a non-linear least-squares fit to the experimental data. The absorption coefficients of the $MgSnN_2$ films were then obtained from the respective best-matched MDFs.

Low-temperature photoluminescence measurements were carried out at 80 K by cooling samples in a liquid-nitrogen cryostat. The layers were excited using the 351 nm ultraviolet line of an Ar-ion laser with a power below 5 mW, moderately focused onto the sample to a spot diameter of approximately 100 μm. The emitted PL signal was analyzed using a monochromator (Jobin Yvon HR460) equipped with a multichannel detector.

Acknowledgements

We thank L. Illés (HUN-REN) for FIB preparation. This work is supported by the Wallenberg Initiative Materials Science for Sustainability (WISE) funded by the Knut and Alice Wallenberg Foundation. We acknowledge additional support by the Swedish Government Strategic Research Area in Materials Science on Functional Materials at Linköping University (Faculty Grant SFO-Mat-LiU No. 2009 00971), the Knut and Alice Wallenberg foundation through the Wallenberg Academy Fellows program (KAW-2020.0196, P.E.), the Swedish Research Council (VR) under Project Nos. 2021–03826, 2025–03680, and 2025–03760 and No. 2023–04993 V.D. acknowledges support by the Knut and Alice Wallenberg Foundation for a Scholar award (Grant No. 2023.0349), and D.Q.T. acknowledges support by the Knut and Alice Wallenberg Foundation for a Postdoctoral Fellowship to Stanford University. B. Pecz acknowledges the support of the NKFIH ADVANCED NKKP 152987 project and A.K. acknowledges the support of the MTA Distinguished Fellowship Program 2024. D.G. thanks the Carl Trygger Foundation for Scientific Research (Grant No. 312449).

Author Contributions

D. Gogova: conceptualization, writing – original draft, project administration, resources, data curation, formal analysis, methodology, investigation, visualization, validation. **D. Tran**: data curation, formal analysis, writing – review and editing, investigation, visualization, validation, software. **V. Stanishev**: data curation, formal analysis, visualization, investigation, writing – review and editing, software. **D. Shafizadeh**: data curation, formal analysis, investigation, writing – review and editing. **C.-L. Hsiao**: data curation, formal analysis, visualization, investigation, writing – review and editing. **M. Kim**: data curation, formal analysis, visualization, investigation, writing – review and editing. **B. Pécz**: data curation, formal analysis, visualization, funding acquisition, resources, project administration, writing – review and editing, supervision, methodology, software, validation. **A. Kovács**: data curation, formal analysis, visualization, investigation, software, resources, writing – review and editing, methodology, validation. **K. Frey**: data curation, formal analysis, visualization, software, resources, writing – review and editing. **A. Sulyok**: data curation, formal analysis, visualization, investigation, software, validation, writing – review and editing. **N. K. Singh**: data curation, formal analysis, investigation, writing – review and editing. **A. Le Febvrier**: data curation, formal analysis, visualization, writing – review and editing, supervision, investigation, funding acquisition, resources, validation, methodology. **P. Eklund**: validation, funding acquisition, resources, writing – review and editing, project administration, supervision, investigation, methodology. **V. Darakchieva**: resources, funding acquisition, validation, writing – review and editing, project administration, supervision.

Conflicts of Interest

The authors declare no conflicts of interest.

Data Availability Statement

The data that support the findings of this study are available from the corresponding author upon reasonable request.

References

1. G. R. Yazdi, P. O. Persson, D. Gogova, et al., "Aligned AlN Nanowires by Self-Organized Vapor–Solid Growth," *Nanotechnology* 20, no. 49 (2009): 495304, https://doi.org/10.1088/0957-4484/20/49/495304.

2. S. V. Ivanov, V. N. Jmerik, T. V. Shubina, et al., "InGaN-Based Epilayers and Quantum Wells With Intense Room-Temperature Photoluminescence in the 500–650 nm Range," *Journal of Crystal Growth* 301–302 (2007): 465–468, https://doi.org/10.1016/j.jcrysgro.2006.09.008.

3. D. Gogova, H. Larsson, R. Yakimova, et al., "Fast Growth of High-Quality GaN," *Physics Status Solidi* 200, no. 1 (2003): 13–17, https://onlinelibrary.wiley.com/doi/abs/10.1002/pssa.200303342.

4. W. Sun, C. K. Tan, and N. Tansu, "III-Nitride Digital Alloy: Electronics and Optoelectronics Properties of the InN/GaN Ultra-Short Period Superlattice Nanostructures," *Scientific Reports* 7, no. 1 (2017): 6671, https://doi.org/10.1038/s41598-017-06889-3.

5. R. Gergova, K. S. A. Butcher, P. W. Binsted, and D. Gogova, "Initial Results for Epitaxial Growth of InN on Gallium Oxide and Improved Migration-Enhanced Afterglow Epitaxy Growth on Gallium Nitride," *Journal of Vacuum Science & Technology B, Nanotechnology and Microelectronics: Materials, Processing, Measurement, and Phenomena* 32, no. 3 (2014): 0312071, https://doi.org/10.1116/1.4874535.

6. T. Malinauskas, K. Jarašiunas, R. Aleksiejunas, et al., "Contribution of Dislocations to Carrier Recombination and Transport in Highly Excited ELO and HVPE GaN Layers," *Physica Status Solidi* 243, no. 7 (2006): 1426–1430.

7. H. Coelho-Júnior, B. G. Silva, C. Labre, R. P. Loreto, and R. L. Sommer, "Room-Temperature Synthesis of Earth-Abundant Semiconductor $ZnSiN_2$ on Amorphous Carbon," *Scientific Reports* 11 (2021): 3248.

8. I. S. Khan, K. N. Heinselman, and A. Zakutayev, "Review of $ZnSnN_2$ Semiconductor Material," *Journal of Physics: Energy* 2 (2020): 032007, https://doi.org/10.1088/2515-7655/ab8b69.

9. F. Deng, H. Cao, L. Liang, et al., "Determination of the Basic Optical Parameters of $ZnSnN_2$," *Optics Letters* 40 (2015): 1282–1285, https://opg.optica.org/ol/abstract.cfm?URI=ol-40-7-1282.

10. A. Bafekry, M. Faraji, and M. M. Fadlallah, et al., "Point Defects in a Two-Dimensional $ZnSnN_2$ Nanosheet: A First-Principles Study on the Electronic and Magnetic Properties," *The Journal of Physical Chemistry C* 125, no. 23 (2021): 13067–13075, https://doi.org/10.1021/acs.jpcc.1c03749.

11. D. Gogova, V. Olsen, C. Bazioti, et al., "High Electron Mobility Single-Crystalline $ZnSnN_2$ on ZnO (0001) Substrates," *CrystEngComm* 22 (2020): 6268–6274, https://doi.org/10.1039/D0CE00861C.

12. V. S. Olsen, V. Øversjøen, D. Gogova, et al., "$ZnSnN_2$ in Real Space and k-Space: Lattice Constants, Dislocation Density, and Optical Band Gap," *Advanced Optical Materials* 9 (2021): 2100015, https://doi.org/10.1002/adom.202100015.

13. A. Nezhdanov, A. Skrylev, D. Shestakov, et al., "Mixed Phase $ZnSnN_2$ Thin Films for Solar Energy Applications: Insight Into Optical and Electrical Properties," *Optical Materials* 144 (2023): 114335, https://doi.org/10.1016/j.optmat.2023.114335.

14. N. Yamada, K. Matsuura, M. Imura, H. Murata, and F. Kawamura, "Composition-Dependent Properties of Wurtzite-Type $Mg_{1+x}Sn_{1-x}N_2$ Epitaxially Grown on GaN(001) Templates," *ACS Applied Electronic Materials* 3 (2021): 1341–1349, https://doi.org/10.1021/acsaelm.0c01115.

15. N. Yamada, M. Mizutani, K. Matsuura, et al., "Band Gap-Tunable (Mg, Zn)SnN_2 Earth-Abundant Alloys With a Wurtzite Structure," *ACS Applied Electronic Materials* 3 (2021): 4934–4942, https://doi.org/10.1021/acsaelm.1c00754.

16. A. Skrylev, A. Nezhdanov, I. Belokon, et al., "Electrophysical Properties of Cation-Disordered $ZnSnN_2$ Films: Temperature Dependences and Thermal Annealing," *Physica B: Condensed Matter* 721 (2026): 418058, https://doi.org/10.1016/j.physb.2025.418058.

17. A. P. Jaroenjittichai and W. R. L. Lambrecht, "Electronic Band Structure of Mg–IV–N_2 Compounds in the Quasiparticle-Self-Consistent GW Approximation," *Physical Review B* 94 (2016): 125201, https://doi.org/10.1103/PhysRevB.94.125201.

18. R. A. Makin, K. York, S. M. Durbin, et al., "Alloy-Free Band Gap Tuning Across the Visible Spectrum," *Physical Review Letters* 122 (2019): 256403, https://doi.org/10.1103/PhysRevLett.122.256403.

19. I. Ho and G. B. Stringfellow, "Solid Phase Immiscibility in GaInN," *Applied Physics Letters* 69 (1996): 2701–2703, https://doi.org/10.1063/1.117683.

20. S. Pleasants, "Overcoming the 'Green Gap'," *Nature Photonics* 7 (2013): 585.

21. B. B. Dumre, D. Gall, and S. V. Khare, "Stability, and Electronic and Optical Properties of Ternary Nitride Phases of $MgSnN_2$: A First-Principles Study," *Journal of Physics and Chemistry of Solids* 153 (2021): 110011, https://doi.org/10.1016/j.jpcs.2021.110011.

22. F. Kawamura, M. Imura, H. Murata, N. Yamada, and T. Taniguchi, "Synthesis of a Novel Rocksalt-Type Ternary Nitride Semiconductor $MgSnN_2$ Using the Metathesis Reaction Under High Pressure," *European Journal of Inorganic Chemistry* 2020 (2020): 418, https://doi.org/10.1002/ejic.202000019.

23. K. R. York, R. A. Makin, N. Senabulya, et al., "Growth Parameter Based Control of Cation Disorder in $MgSnN_2$ Thin Films," *Journal of Electronic Materials* 50 (2021): 2949–2955, https://doi.org/10.1007/s11664-020-08708-4.

24. F. Alnjiman, A. Virfeu, and D. Pilloud, "Theoretical and Experimental Approaches for the Determination of Functional Properties of $MgSnN_2$ Thin Films," *Solar Energy Materials and Solar Cells* 244 (2022): 111797, https://doi.org/10.1016/j.solmat.2022.111797.

25. K. Makiuchi, F. Kawamura, H. Murata, and N. Yamada, "Pressure-Induced Transition From Wurtzite and Epitaxial Stabilization for Thin Films of Rocksalt $MgSnN_2$," *Chemistry of Materials* 35, no. 5 (2023): 2095–2106, https://doi.org/10.1021/acs.chemmater.2c03671.

26. T. Malinauskas, R. Aleksiejunas, K. Jarašiunas, et al., "All-Optical Characterization of Carrier Lifetimes and Diffusion Lengths in MOCVD-, ELO-, and HVPE- Grown GaN," *Journal of Crystal Growth* 300 (2007): 223–227, https://doi.org/10.1016/j.jcrysgro.2006.11.014.

27. P. Kuehne, N. Armakavicius, A. Papamichail, et al., "Enhancement of 2DEG Effective Mass in $AlN/Al_{0.78}Ga_{0.22}N$ High Electron Mobility Transistor Structure Determined by THz Optical Hall Effect," *Applied Physics Letters* 120, no. 25 (2022): 253102, https://doi.org/10.1063/5.0087033.

28. V. Stanishev, N. Armakavicius, D. Gogova, et al., "Low Al-Content n-type $Al_xGa_{1-x}N$ Layers With a High-Electron-Mobility Grown by Hot-Wall Metalorganic Chemical Vapor Deposition," *Vacuum* 217 (2023): 112481, https://doi.org/10.1016/j.vacuum.2023.112481.

29. A. L. Greenaway, A. L. Loutris, K. N. Heinselman, et al., "Combinatorial Synthesis of Magnesium Tin Nitride Semiconductors," *Journal of the American Chemical Society* 142 (2020): 8421–8430, https://doi.org/10.1021/jacs.0c02092.

30. D. Gogova, H. Larsson, A. Kasic, et al., "High-Quality 2" Bulk-Like Free-Standing GaN Grown by HydrideVapour Phase Epitaxy on a Si-doped Metal Organic Vapour Phase Epitaxial GaN Template With an Ultra Low Dislocation Density," *Japanese Journal of Applied Physics* 44, no. 3 (2005): 1181–1185, https://doi.org/10.1143/JJAP.44.1181.

31. H. Amano, N. Sawaki, I. Akasaki, and Y. Toyoda, "Metalorganic Vapor Phase Epitaxial Growth of a High Quality GaN Film Using an AlN Buffer Layer," *Applied Physics Letters* 48, no. 5 (1986): 353–355, https://doi.org/10.1063/1.96549.

32. D. Gogova, D. Q. Tran, V. Stanishev, et al., "High Crystalline Quality Homoepitaxial Si-Doped β-Ga_2O_3 (010) Layers With Reduced Structural Anisotropy Grown by Hot-wall MOCVD," *Journal of Vacuum Science & Technology A* 42 (2024): 022708, https://doi.org/10.1116/6.0003424.

33. P. Petrov, H. Guhl, and W. Miller, "First Atomistic Studies of Epitaxial Growth of $Na_{0.5}Bi_{0.5}TiO_3$ on $SrTiO_3$," *Physica Status Solidi* 245, no. 12 (2008): 2649–2656.

34. P. Petrov and D. Gogova, "Surface Roughness Evolution in a Solid-On-Solid Model of Epitaxial Growth," *Applied Physics A* 118 (2015): 337–343, https://link.springer.com/article/10.1007/s00339-014-8736-1.

35. P. Petrov and W. Miller, "A New Kinetic Monte Carlo Method for the Thin Film Growth of Perovskites," *Surface Review and Letters* 16, no. 06 (2009): 909–916, https://doi.org/10.1142/S0218625X09013475.

36. D. Gogova, M. Schmidbauer, and A. Kwasniewski, "Homo- and Heteroepitaxial Growth of Sn-Doped β-Ga_2O_3 Layers by MOVPE," *CrystEngComm* 17, no. 35 (2015): 6744–6752, https://doi.org/10.1039/C5CE01106J.

37. S. Yata, M. Mizutani, K. Makiuchi, et al., "Electron Transport Properties in Degenerate Magnesium Tin Oxynitride ($Mg_{1-x}Sn_{1+x}N_{2-2y}O_{2y}$) With Average Wurtzite Structure," *Journal of Applied Physics* 131 (2022): 075302, https://doi.org/10.1063/5.0077925.

38. D. Han, S. S. Rudel, W. Schnick, and H. Ebert, "Self-Doping Behavior and Cation Disorder in $MgSnN_2$," *Physical Review B* 105 (2022): 125202, https://doi.org/10.1103/PhysRevB.105.125202.

39. M. Kute, Z. Deng, S. Chae, E. Kioupakis, et al., "Cation-Size Mismatch as a Predictive Descriptor for Structural Distortion, Configurational Disorder, and Valence-Band Splitting in II-IV-N_2 Semiconductors," *Applied Physics Letters* 119 (2021): 132104, https://doi.org/10.1063/5.0062942.

40. S.-Y. Zhuo, X.-C. Liu, T.-X. Xu, C.-F. Yan, and E.-W. Shi, "Strong Correlation Between B-Al-N Doping Concentration Fluctuation and Photoluminescence Effects of f-SiC," *American Institute of Physics Advances* 8 (2018): 075130, https://doi.org/10.1063/1.5044492.

41. A. Le Febvrier, L. Landalv, T. Liersch, D. Sandmark, P. Sandström, and P. Eklund, "An Upgraded Ultra-High Vacuum Magnetron-Sputtering System for High-versatility and Software-Controlled Deposition," *Vacuum* 187 (2021): 110137, https://doi.org/10.1016/j.vacuum.2021.110137.